Increasing Frequency of Extremely Severe Cyclonic Storms over the Arabian Sea

Hiroyuki Murakami[1,2], Gabriel A. Vecchi[3,4], and Seth Underwood[1]

[1]National Oceanic and Atmospheric Administration/Geophysical Fluid Dynamics Laboratory, Princeton, NJ, USA

[2]Atmospheric and Oceanic Sciences Program, Princeton University, Princeton, NJ, USA

[3]Department of Geosciences, Princeton University, Princeton, NJ, USA

[4]Princeton Environmental Institute, Princeton University, Princeton, NJ, USA

Revised on 27 Sep 2017
Revised on 12 Aug 2017
Submitted to *Nature Climate Change* on 19 May 2017

Key words: global warming, Arabian Sea, and extremely severe cyclonic storms

---

Corresponding author address: Hiroyuki Murakami, NOAA/GFDL, 201 Forrestal Rd., Princeton, NJ 08540-6649
E-mail: hir.murakami@gmail.com
Tel: +1-609-452-5824

In 2014 and 2015, post-monsoon extremely severe cyclonic storms (ESCS)—tropical storms with lifetime maximum winds greater than 46 m s^{-1} (WMO[1])—were first observed over the Arabian Sea (ARB), causing widespread damage[2]. However, it is unknown to what extent this abrupt increase in post-monsoon ESCSs can best be linked to anthropogenic warming, natural variability, or stochastic behaviour. Here, using a suite of high-resolution model experiments[3], we show that anthropogenic forcing has likely increased the probability of late-season ECSCs occurring in the ARB since the preindustrial era. However, the timing of observed late-season ESCSs in 2014 and 2015 was likely due to stochastic processes. It is further shown that natural variability played a minimal role in the observed increase of ESCSs. Thus, continued anthropogenic forcing will further amplify the risk of cyclones in the ARB, with corresponding socio-economic implications.

In 2014, the first ESCS (Cyclone Nilofar) was recorded in the ARB (west of 77.5ºE in the North Indian Ocean) during the post-monsoon season (October–December)(Fig. 1a). In the following year, two more ESCSs (Cyclones Chapala and Megh) were again observed during the post-monsoon season in the ARB (Fig. 1a). This was the first instance that more than one ESCS was observed within one year in the ARB (Fig. 1b). These recent severe tropical storms in the ARB have attracted considerable attention from the scientific community, as well as broader society, in terms of the extent to which they were made more likely by anthropogenic forcing, as opposed to intrinsic natural variability. A recent study[4] reported that the increase in anthropogenic black carbon and sulphate emissions might have led to the increase in mean storm intensity in the ARB through a weakening of vertical wind shear (V_s, wind speed difference between the upper and lower troposphere), especially during the pre-monsoon season of April–

June. The suggested physical mechanism behind this change is that the observed increase in anthropogenic aerosols in the lower troposphere leads to a reduction in surface insolation in the North Indian Ocean, which in turn leads to a decrease in the meridional gradient of sea surface temperature (SST). This decreased meridional gradient further leads to a weakening of the South Asian Monsoon circulation through the thermal wind relationship, which causes a weakening of the V_s. On the other hand, another study[5] argued that the recent increase in pre-monsoon tropical storm intensity in the ARB is mainly being caused by an earlier onset of the South Asian Monsoon, affected by a reversal in the phase of the Pacific Decadal Oscillation (PDO) around 1997. Overall, consensus has not been reached regarding the main cause of the recent increase in pre-monsoon storm intensity in the ARB. Alongside this debate, the recent unprecedented occurrence of ARB ESCSs in 2014 and 2015 calls for additional focus on the post-monsoon season. The observed tropical storm activity in the ARB shows a bimodal annual frequency distribution, peaking during the pre-monsoon and post-monsoon season[6]. However, the observed seasonal large-scale conditions are fundamentally different between the two seasons in terms of the direction of low-level wind and V_s (Supplementary Fig. 1). Therefore, the effect of anthropogenic forcing on storm activity could also be different between the two seasons.

Meanwhile, long-term analysis of the observed storm record is uncertain given a very limited period of reliable satellite-based data covering the ARB. There was no satellite that covered the entire ARB before 1998, and so the storm intensity might have been underestimated due to the oblique view offered by adjacent satellites[7]. However, Fig. 1b reveals that, even after 1998, ESCSs were not observed in the post-monsoon season until 2014, drawing interest as to whether the increase is physically related to anthropogenic warming; indeed, several studies have consistently reported that anthropogenic global warming has increased the mean storm intensity[8].

As a complement to the limited observational record, we use a suite of numerical climate model experiments to address the plausibility and causes of the recent increase in post-monsoon ESCSs in the ARB. The ARB poses a challenge for numerical climate modelling, not only because of its relatively small domain size, but also the complex climatic conditions and influences in the region and the general rarity of tropical storm genesis in the ARB. On average, about 1.7 (0.6 during the pre-monsoon season and 0.9 during the post-monsoon season) tropical storms (lifetime maximum surface wind speed ≥17.5 m s^{-1}) formed in a year in the ARB during 1979–2015, which is only about 2% of the storm frequency globally. Thus, models with high resolution, fidelity in their climate simulations, and ability to produce multi-centennial integrations for the provision of a satisfactory signal-to-noise ratio, are required. However, the limited reliability of observations makes it difficult to evaluate model simulations in terms of the interannual variation of storm frequency at the multi-decadal time scale. Although many state-of-the-art models succeed in simulating the observed year-by-year variation of tropical storm frequency in the North Atlantic[3,9–10], they commonly fail to reproduce the equivalent in the North Indian Ocean[10–12]. This failure may be due to the imperfect representation of variability in models, the inhomogeneous observed storm record, difficulties with tropical cyclone (TC) detection methods in distinguishing TCs from low-pressure systems (e.g., monsoon depressions)[13], or the limited predictability of TC frequency over the region. Another problem with model simulations is that the horizontal resolution of the climate models is still insufficient to reproduce observations of intense storms. Several climate models have been used to conduct future climate projections, and the results commonly suggest that the frequency of weak (intense) storms will decrease (increase) globally in the future[8]. However, most models underestimate the observed TC intensity, especially for major hurricanes (maximum surface wind speed ≥50 m s^{-1})[8]. Moreover, little is known about the change in TC activity over the ARB. Murakami et al.[12] conducted multi-physics and multi-SST ensemble climate projections under the IPCC A1B scenario[14] using a 60-km-mesh atmospheric model. The results showed that the mean locations of tropical storms may shift westwards over the North Indian Ocean during the post-monsoon season, leading to an increased (decreased) frequency of tropical storms over the ARB (Bay of Bengal). However, little is known about possible change in intense storms like ESCSs. The present study aims to bridge that gap.

We recently developed a new high-resolution global coupled model at the Geophysical Fluid Dynamics Laboratory called HiFLOR that broadly reproduces the observed year-by-year variations of the frequency of Category 4 and 5 (C45) hurricanes (maximum wind speed ≥58 m s^{-1}) in the North Indian Ocean (r≈0.4) as well as in other ocean basins[3,15]. Moreover, HiFLOR simulates the climatological spatial distribution of ESCSs over the ARB reasonably well, as compared with observations, based on a present-day control simulation (Supplementary Fig. 2). Therefore, it is feasible to investigate the factor(s) responsible for the recent increase in ESCSs using HiFLOR. In this study, through a suite of climate simulations, we specifically investigate if the recent observed increase in ESCSs is due to anthropogenic global warming or natural variability.

To estimate the impact of anthropogenic forcing on the frequency of ESCSs over the ARB, we conducted a series of control simulations prescribing past levels of anthropogenic and natural forcing (Methods). Specifically, we conducted 1860Cntl, 1940Cntl, 1990Cntl, and 2015Cntl experiments in which anthropogenic forcing was fixed at the years of 1860, 1940, 1990, and 2015, respectively (Methods). Figure 2 shows the projected change in the mean ESCS density for each experiment and for each season relative to 1860Cntl. Although the model response in 1940Cntl is smaller and not statistically significant for all seasons, the 1990Cntl and 2015Cntl results show significant increases in the occurrence of ESCSs over the ARB during the post-monsoon season only. These projected increases coincide with the recent observed increase in ESCSs over the ARB during the post-monsoon season.

Following Murakami et al.[16, 17], we estimated the potential influence of anthropogenic forcing on the frequency of occurrence of ESCSs by computing the empirical probability of exceedance (Methods). In this study, we focus on *P(1)*, representing the probability of occurrence of a year with one or more ESCSs during the post-monsoon season over the ARB. The gray bars along with the box plots in Fig. 3a clearly indicate a projected significant increase in *P(1)* for 1990Cntl and 2015Cntl relative to 1860Cntl and 1940Cntl. The fraction of attributable risk (FAR, Methods) for 2015Cntl and 1990Cntl is 64% and 57%, respectively, suggesting that the increase in the probability of occurrence is attributable to the increase in anthropogenic forcing. Note that we repeated the same analysis but for weak storms (< 46 m s^{-1}), and the results showed no significant changes among the control simulations during the post-monsoon season (Supplementary Fig. 3).

We further computed the conditional *P(1)*—namely, $P(1|Y_{\pm})$ under any phase of a natural mode of variability (i.e., Y_{+} or Y_{-})—to estimate impact of natural variability on the changes in *P(1)* (Methods). The colored bars in Fig. 3b reveal the extent to which the different phases of natural variability exert variation in the probability of exceedance. Overall, we obtained diverse and inconsistent results among the control experiments. For example, 2015Cntl (1940Cntl) shows the highest probability during the positive (negative) phase of the PDO. The reason for these diverse results—possibly related to whether the 200–300 year records are short enough to alias the noise and the impact of these internal climate modes on ESCS activity being weak, or whether the impact of the PDO is sensitive to the base state—remains unclear. The relatively shorter colored bars for the longest 600-year 1860Cntl (Fig. 3b) lend weight to the hypothesis that the impact of these potentially predictable modes of climate variability on ESCS activity is weak, suggesting that natural variations in post-monsoon ESCS activity may be largely unpredictable. However, overall, we could not find any clear and robust dependence of the probability of occurrence on these modes of natural variability.

To address the physical mechanism behind the projected increase in ESCSs in the post-monsoon season, we preliminarily investigated several large-scale parameters associated with storm activity. Among them, the projected changes in SST and V_s appear to be responsible for the increase in ESCSs. Figure 4 highlights a marked sea surface warming over the ARB (Fig. 4a), with larger warming relative to the mean change in the tropics (RSST, Supplementary Fig. 4a), as well as a significant weakening of V_s over the ARB (Fig. 4b). Several previous studies have reported projected increases in TC density and maximum potential intensity where the SST increases more than in other open oceans[10,18–21]. Similar spatial patterns of the projected changes in the large-scale parameters could also be obtained through future projections with CMIP3 models[19] and CMIP5 models[22]. Figures 4c and d show the ensemble mean of the projected changes in SST (Fig. 4c) and V_s (Fig. 4d) in 22 CMIP5 models under the RCP8.5 (2006–2025) scenario relative to the pre-industrial control experiments (500 years). The CMIP5 models show larger warming over the ARB (Supplementary Fig. 4b) that is consistent with the projections by HiFLOR. A larger ARB warming relative to other open oceans has also been reported in century-scale observations[18], in which the largest projected and observed trends in relative SST and potential intensity were found over the tropical part of this region. Moreover, the CMIP5 models also show relatively weaker V_s for the region's increase in ESCSs during the post-monsoon season (Fig. 4d). Similar changes are also projected in the future by the CMIP5 models (Figs. 4e and f), implying a continuing increase in ARB ECSCs during the post-monsoon season due to weaker shear and warmer SSTs in the future. Similar changes in SST and RSST are also projected during the pre-monsoon season (Supplementary Figs. 4d–f, 5, 6a and b). However, we could not find any significant decreases in V_s during the pre-monsoon season over the ARB domain where ESCSs increased (Supplementary Figs. 5 and 6c). Consequently, the pre-monsoon season shows a smaller projected increase in *P(1)* relative to the post-monsoon season (Supplementary Fig. 7).

It is possible that the projected changes in V_s are related to the changes in either the strength or the timing of the onset/retreat of the Indian monsoon. By analyzing the changes in the Indian monsoon circulation (Methods), we found that the projected weakening of the winter monsoon circulation is key for the weakening of V_s during the post-monsoon season. Previous literature has also reported that state-of-the-art climate models commonly project a weakening of the Indian monsoon circulation in experiments run with anthropogenic forcing[23]. On the other hand, we could not find any significant difference in the timing of monsoon onset or withdrawal (Supplementary Fig. 11), although IPCC[23] reported that model agreement is high on an earlier onset and later retreat (i.e., longer duration) in future projections. Uncertainty remains in this regard.

As reviewed above, Evan et al.[4] reported that the recent increase in anthropogenic aerosols caused an increase in TC intensity over the ARB through a weakening of V_s. Accordingly, we investigated the influence of aerosols on the frequency of ESCSs. We conducted an additional idealized experiment in which the simulation settings were identical to those in the 2015Cntl, except the anthropogenic aerosols (i.e., black carbon, organic carbon, and sulfate, etc) were prescribed at the 1860 level. The increase in aerosols causes a small increase in ESCSs [labeled as "2015 Cntl (1860Aero)" in Fig. 3], which is consistent with a previous study[4]. However, the projected impact of aerosols on ESCSs may be underestimated in the model because the model underestimates direct radiative forcing by aerosols over the ARB compared with observations, especially at the surface (Supplementary Fig. 12). Moreover, the model does not include indirect effects of aerosols, and so the aerosol forcing is of smaller amplitude than in observations. Further refinement of the model's physics is necessary in the future to estimate the effect of aerosols on ECSCs with more precision.

Overall, the suite of high-resolution model experiments carried out in this study indicate that anthropogenic global warming has increased the probability of post-monsoon ESCSs over the ARB, and is one of the major contributors to the recent (2014 and 2015) observations in this regard. The specific occurrence in those years, but not in other years in recent decades, reflects the interplay between climate change, climate variability and weather. However, the climate simulations do not show any consistent dependency on the phases of natural variability that we explored. Therefore, we believe that stochastic factors (i.e., "weather noise") or unexplored modes of climate variability were key to the precise timing of these events.

Acknowledgments

The authors thank Dr. Thomas L. Delworth and Dr. Lakshmi Krishnamurthy for their suggestions and comments. H.M. appreciates Dr. Pang-Chi Hsu for her support of editorial service. This report was prepared by H.M. under award NA14OAR4830101 from the National Oceanic and Atmospheric Administration, U.S. Department of Commerce. The statements, findings, conclusions, and recommendations are those of the authors and do not necessarily

reflect the views of the National Oceanic and Atmospheric Administration, or the U.S. Department of Commerce.

Author Contributions

H.M. designed the study, carried out the experiments, and analyzed the results. G.A.V. and S.W. carried out the experiments and made comments on the manuscript.

Corresponding Author

Correspondence and requests for materials should be addressed to H.M.

Competing Financial Interests

The authors declare no competing financial interests.

Methods (On-Line)

a. Observed data

We used the U.S. Department of Defense Joint Typhoon Warning Center Best Track Database[25], as archived in the International Best Track Archive for Climate Stewardship[26], for the period 1998–2015. The 2016 TC data were complemented in this study by the best track data openly available on the Unisys Corporation website[27]. We also used the UK Met Office Hadley Centre SST product (HadISST1.1)[28] as the observed SST. For the atmospheric data, the Japanese 55-year Reanalysis (JRA-55)[29] was utilized.

b. Control experiments

We generated a 600-year control climate simulation using HiFLOR by prescribing radiative forcing and land-use conditions representative of the year 1860 (1860Cntl). The fixed forcing agents for the control simulations were atmospheric CO_2, CH_4, N_2O, halons, tropospheric and stratospheric O_3, anthropogenic tropospheric sulfates, black and organic carbon, and solar irradiance. We also conducted 1940, 1990, and 2015 control simulations by prescribing the anthropogenic forcing fixed at the levels in those years. Due to limited computational resource, we ran 1940Cntl, 1990Cntl, and 2015Cntl for 200, 300, and 200 years, respectively. However, the basic conclusions were retained even we used 200 years for all the control simulations.

c. Empirical probability of exceedance and FAR

To estimate the potential probability of occurrence for the extreme ESCS-incidence years like 2015, we examined the empirical probability of exceedance for the frequency:

$$P(x) = \frac{Number\ of\ years\ with\ ESCS\ number \geq x}{Total\ number\ of\ years}$$

(1),

where x is the seasonal mean number of ESCSs in a year. For the control experiments, we compute $P(x)$ using all 600, 200, 300, and 200 simulated years for 1860Cntl, 1940Cntl, 1990Cntl and 2015Cntl, respectively. To elucidate the inter-centennial (inter-decadal) variability, we computed $P(x)$ for each 50-year (19-year) period.

The FAR[30] was computed for the estimation of the impact of anthropogenic forcing. FAR is defined as follows:

$$FAR(x) = \frac{P(x|E_1) - P(x|E_0)}{P(x|E_1)}$$

(2),

where E_1 is the anthropogenic warming condition (either for 1940Cntl, 1990Cntl or 2015Cntl), whereas E_0 stands for natural forcing alone (1860Cntl). FAR ranges from $-\infty$ (not attributable) to 100% (attributable).

To address the impact of any phase of natural variability, we can also estimate the conditional probability of exceedance $P(x|Y_\pm)$ under any phase of a natural mode of variability (i.e., Y_+ or Y_-). Here, we investigated the difference in $P(1)$ between positive and negative phases of the El Niño–Southern Oscillation (ENSO; based on the Niño-3.4 index), Pacific Meridional Mode (PMM)[31], PDO[32], and Indian Ocean Dipole (IOD)[33]. These indices were selected because they may potentially influence the frequency of occurrence of ESCSs, based on the SST regression map (Supplementary Fig. 8). The detailed computations for these indices are documented in Murakami et al.[16,17]. In simple terms, ENSO represents the interannual variation of tropical eastern Pacific surface warming concurrent with basin-wide warming in the Indian Ocean; PMM represents the interannual variation of SST warming/cooling over the subtropical eastern Pacific, whereas the PDO represents the interannual and decadal variation; and the IOD represents the interannual variation of the meridional SST contrast in the Indian Ocean. We defined a positive (negative) phase of natural variability when the index was greater than or equal to +0.75σ (less than or equal to −0.75σ). The other years were defined as neutral years. $P(x|Y_{\pm})$ was computed using the years under each phase.

d. Projected changes in the Indian monsoon circulation

The projected decrease in V_s may be related to the changes in the strength or the onset of the Indian monsoon. Supplementary Fig. 9 clarifies the changes in the lower/upper tropospheric winds during October–December between 1860Cntl and 2015Cntl. October–December is the beginning of the South Indian winter monsoon as characterized by northeasterly (southwesterly) winds in the lower (upper) troposphere over the ARB (Supplementary Figs. 1d and e). The projected difference between 2015Cntl and 1860Cntl indicates a weakening of the winter monsoon circulation: a southwesterly (northeasterly) anomaly in the lower (upper) troposphere over the ARB (Supplementary Figs. 9c–d), which leads to a weakening of V_s. On the other hand, April–June is the transition season from winter monsoon to summer monsoon, as characterized by southwesterly winds in the lower troposphere over the ARB (Supplementary Fig. 1a), which is the opposite to October–December (Supplementary Fig. 1d). The projected difference between 2015Cntl and 1860Cntl shows southwesterly flow in the lower troposphere during April–June (Supplementary Fig. 10c). Unlike October–December, the direction of wind change is along the climatological mean wind direction (Supplementary Figs. 10a and c). Moreover, there is less change in the wind in the upper troposphere over the region where ECSCs develop during April–

June (Supplementary Fig. 10d), which is one of the major factors for the less pronounced changes in V_s during April–June relative to October–December (Supplementary Fig. 6c).

There are various indices that can be used to measure the Indian monsoon. We used the Dynamic Indian Monsoon Index (DIMI) of Wand & Fan[34]. The index is computed by the area-mean differences in zonal wind at 850hPa between region A (5–15°N, 40–80°E) and B (20–30°N, 70–90°E), denoted in Supplementary Fig. 9a. The index is proportional to circulation strength, with a positive (negative) value meaning a summer (winter) monsoon phase. We computed the DIMI using the daily data for each 2015Cntl and 1860Cntl run. Also, the DIMI was smoothed with a 15-day running average. Supplementary Fig. 11 shows the smoothed climatological daily DIMI by 2015Cntl (red) and 1860Cntl (blue), separately. The figure indicates a weakening of both the summer Indian monsoon and winter monsoon from 1860Cntl to 2015Cntl. Although the projected DIMI change is significant during the post-monsoon season (October–December), there is no significant difference at 95% confidence level in the index during the pre-monsoon season (April–June) (Supplementary Table 1). The change of sign occurs almost at the same time between 1860Cntl and 2015Cntl, indicating the monsoon onset (or withdrawal) occurs almost at the same time in these experiments (Supplementary Fig. 11).

e. Data availability

The source code of the climate model can be found at https://www.gfdl.noaa.gov/cm2-5-and-flor/. The data that support the findings of this study are available from the corresponding author upon request.

References

1. WMO. Tropical cyclone operational plan for the Bay of Bengal and Arabian Sea, World Meteorological Organization Tech. Tropical Cyclone Programme Rep. TCP-21, WMO/TD-84, 112pp. [Available online at https://www.wmo.int/pages/prog/www/tcp/documents/TCP-21Edition2015_final.pdf] (2015).

2. Kruk, M. C. Tropical Cyclones, North Indian Ocean. [in " State of the Climate in 2015"]. *Bull. Amer. Meteor. Soc.*, **97(8),** S114–S115 (2016).

3. Murakami, H. *et al*. Simulation and prediction of Category 4 and 5 hurricanes in the high-resolution GFDL HiFLOR coupled climate model. *J. Climate*, **28**, 9058–9079 (2015).

4. Evan, A.T., J.P. Kossin, C.E. Chung, & V. Ramanathan. Arabian Sea tropical cyclones intensified by emissions of black carbon and other aerosols. *Nature,* **479,** 94–97 (2011).

5. Wang, B., S. Xu, & L. Wu. Intensified Arabian Sea tropical storms. *Nature,* **489,** E1–E2 (2012).

6. Evan, A.T. & S. J. Camargo. A climatology of Arabian Sea cyclonic storms. *J. Climate*, **24,** 140–158 (2011).

7. Kossin, J.P., T. L. Olander, & K. R. Knapp. Trend analysis with a new global record of tropical cyclone intensity. *J. Climate*, **26,** 9960–9976 (2013).

8. Knutson, T., J. L. McBride, J. Chan, K. Emanuel, G. Holland, C. Landsea, I. Held, J. P. Kossin, A. K. Srivastava, & M. Sugi. Tropical cyclones and climate change. *Nat. Geosci*., **3**, 157–163 (2010).

9. LaRow, T. E., Y.-K. Lim, D. W. Shin, E. P. Chassignet, & S. Cocke. Atlantic basin seasonal hurricane simulations. *J. Climate,* **21,** 3191–3206 (2008).

10. Zhao, M., I. M. Held, S.-J. Lin, & G. A. Vecchi. Simulations of global hurricane climatology, interannual variability, and response to global warming using a 50km resolution GCM. *J. Climate*, **22,** 333–363 (2009).

11. Manganello, J.V. *et al.* Tropical cyclone climatology in a 10-km global atmospheric GCM: Toward weather-resolving climate modeling. *J. Climate*, **24,** 3867–3893 (2012).

12. Murakami, H., M. Sugi, & A. Kitoh. Future changes in tropical cyclone activity in the North Indian Ocean projected by high-resolution MRI-AGCMs. *Clim. Dyn.*, **40(7-8)**, 1949–1968 (2013).

13. Murakami, H. *et al*. Future changes in tropical cyclone activity projected by the new high-resolution MRI-AGCM. *J. Climate* **25,** 3237–3260 (2012).

14. IPCC. Climate change 2007: The physical science basis. Contribution of Working Group I to the Fourth Assessment Report of the Intergovernmental Panel on Climate Change, Cambridge University Press, 996 pp (2007).

15. Murakami, H., G. A. Vecchi, G. Villarini, T. L. Delworth, R. Gudgel, S. Underwood, X. Yang, W. Zhang & S. Lin. Seasonal forecasts of major hurricanes and landfalling tropical cyclones using a high-resolution GFDL coupled climate model. *J. Climate*, **29,** 7977–7989 (2016).

16. Murakami, H., G. A. Vecchi, T. L. Delworth, K. Paffendorf, R. Gudgel, L. Jia, & F. Zeng. Investigating the influence of anthropogenic forcing and natural variability on the 2014 Hawaiian hurricane season. [in "Explaining Extremes of 2014 from a Climate Perspective"]. *Bull. Amer. Meteor. Soc.*, S115–S119 (2015).

17. Murakami, H., G. A. Vecchi, T. L. Delworth, A. T. Wittenberg, S. Underwood, R. Gudgel, X. Yang, L. Jia, F. Zeng, K. Paffendorf, & W. Zhang. Dominant role of subtropical

Pacific warming in extreme eastern Pacific hurricane seasons: 2015 and the future. *J. Climate*, **30,** 243–264 (2017).

18. Vecchi, G. A. & B.J. Soden. Effect of remote sea surface temperature change on tropical cyclone potential intensity. *Nature,* **450,** 1066–1071 (2007).

19. Vecchi, G. A. & B.J. Soden. Increased tropical Atlantic wind shear in model projections of global warming. *Geophys. Res. Lett.,* **34,** L08702 (2007).

20. Sugi M, H. Murakami, & J. Yoshimura. A reduction in global tropical cyclone frequency due to global warming. *SOLA*, **5,**164–167 (2009).

21. Murakami, H., R. Mizuta, & E. Shindo. Future changes in tropical cyclone activity projected by multi-physics and multi-SST ensemble experiments using the 60-km-mesh MRI-AGCM. *Clim. Dyn.*, **39(9-10)**, 2569–2584 (2012).

22. Taylor, K. E., R. J. Stouffer, & G. A. Meehl. An overview of CMIP5 and the experiment design. *Bull. Amer. Meteor. Soc.*, **93,** 485–498 (2012).

23. IPCC. Climate Change 2013. The Physical Science Basis. Contribution of Working Group I to the Fifth Assessment Report of the Intergovern-mental Panel on Climate Change [Stocker, T.F., D. Qin, G.-K. Plattner, M. Tignor, S.K. Allen, J. Boschung, A. Nauels, Y. Xia, V. Bex and P.M. Midgley (eds.)]. Cambridge University Press, Cambridge, United Kingdom and New York, NY, USA, 1535 pp (2013).

24. Murakami, H., B. Wang, T. Li, & A. Kitoh. Projected increase in tropical cyclones near Hawaii. *Nat. Climate Change*, **3,** 749–754 (2013).

25. Chu, J.-H., C.R. Sampson, A.S. Levin & E. Fukada. The Joint Typhoon Warning Center tropical cyclone best tracks 1945–2000, Joint Typhoon Warning Center Rep., Pearl

Harbor, HI, 22pp. [available online at http://www.usno.navy.mil/NOOC/nmfc-ph/RSS/jtwc/best_tracks/TC_bt_report.html], (2002)

26. Knapp, K. R., M. C. Kruk, D. H. Levinson, H. J. Diamond, & C. J. Neuman. The international best track archive for climate stewardship (IBTrACS): Unifying tropical cyclone best track data, *Bull. Amer. Meteor. Soc.*, **91**, 363–376 (2010).

27. Unisys. Unisys weather hurricane tropical data. [available online at http://weather.unisys.com/hurricane/], (2017)

28. Rayner, N. A., D. E. Parker, E. B. Horton, C. K. Folland, L. V. Alexander, & D. P. Rowell. Global analysis of sea surface temperature, sea ice, and night marine air temperature since the late nineteenth century. *J. Geophys. Res*., **108**, 4407 (2003).

29. Kobayashi, S. *et al*. The JRA-55 reanalysis: General specifications and basic characteristics. *J. Meteor. Soc. Japan*, **93**, 5–48 (2015).

30. Jaeger, C.C., J. Krause, A. Haas, R. Klein, & K. Hasselmann. A method for computing the fraction of attributable risk related to climate damages. *Risk Analysis,* **28,** 815–823 (2008).

31. Chiang, J. C. H., & D. J. Vimont. Analogous Pacific and Atlantic meridional modes of tropical atmosphere–Ocean variability *J. Climate*, **17,** 4143–4158 (2004).

32. Mantua, N. J., S.R. Hare, Y. Zhang, J. M. Wallace, & R. C. Francis. A Pacific interdecadal climate oscillation with impacts on salmon production. *Bull. Amer. Meteor. Soc.,* **78,** 1069–1079 (1997).

33. Saji, N.H., B. N. Goswami, P. N. Vinayachandran, & T. Yamagata. A dipole mode in the tropical Indian Ocean. *Nature,* **401,** 360–363 (1999).

34. Wang, B., & Z. Fan. Coice of south Asian summer monsoon indices. *Bull. Amer. Meteor. Soc.,* **80,** 629–638 (1999).

List of Figures

FIG. 1: Observed ESCSs. (a) Observed ESCSs [Nilofar (blue), Chapala (green), and Megh (black)] during the post-monsoon season in 2014 and 2015, along with the observed linear trend in SST (K per 50 years; shading). (b) Observed number of ESCSs over the ARB for each month for the period 1998–2016.

FIG. 2: Projected changes in the seasonal mean density of ESCSs. Projected changes in the seasonal mean density of ESCSs by 1940Cntl relative to 1860Cntl during the (a) pre-monsoon season (Apr–Jun), (b) peak monsoon season (Jul–Sep), and (c) post-monsoon season (Oct–Dec). (d–f) As in (a–c), but for 1990Cntl. (g–i) As in (a–c), but for 2015Cntl. Cross marks indicate the projected change relative to 1860Cntl is statistically significant at the 99% confidence level or above (boot strap method proposed by Murakami et al.[24]). Units: $100 \times$ number year^{-1}. The black box highlights the domain of significant change in the post-season over the ARB.

FIG. 3 Projected probability of exceedance of ESCSs over the ARB during October–December for each experiment. (a) *P(1)*, denoting the probability of occurrence of a year with the ESCS number greater than or equal to one during October–December, obtained by each control experiment using all simulation years (gray bars). The box plots represent uncertainty in *P(1)*. The boxes represent the range of the 10% and 90% quantiles of *P(1)* computed from 50-year periods; the horizontal lines show the median value; and the dashed bars show the 10% and 90% quantiles computed from 19-year periods. Red dots represent the FAR relative to 1860Cntl. (b) Gray bars are the same as in (a). Colored bars show the range of conditional *P(1)* induced by natural variability. The marks +, – and *N* indicate *P(1)* under the condition of a positive phase, negative phase, and neutral phase of natural variability, respectively. Evaluated natural variabilities are ENSO (blue), PMM (orange), PDO (green), and IOD (red). A positive (negative) phase is defined as when a climate index is greater than or equal to +0.75 (less than or equal to −0.75) standard deviation. Units: %.

FIG. 4: Projected changes in seasonal mean SST and V_s. (a) Projected change in seasonal mean SST [K] by 2015Cntl relative to 1860Cntl for October–December. (b) As in (a), but for V_s [m s^{-1}]. (c, d) As in (a, b), but for the ensemble mean of 22 CMIP5 models under the RCP8.5 scenario (2006–2025) relative to those of the pre-industrial control experiments (500 years). (e, f) As in (c, d), but for the mean difference between 2080–2099 and 2006–2025 projected by 36 CMIP5 models under the RCP8.5 scenario. The green rectangle is the domain over the ARB where ESCSs increased.

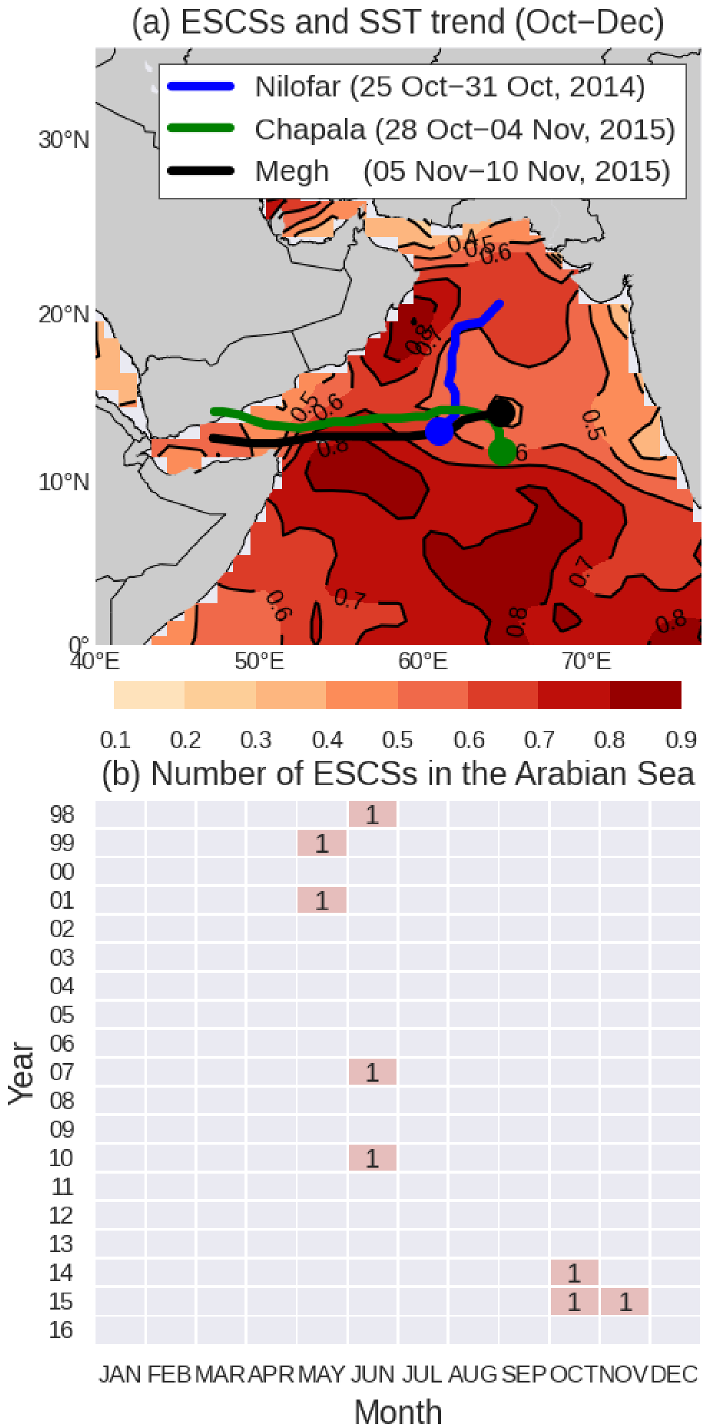

FIG. 1: Observed ESCSs. (a) Observed ESCSs [Nilofar (blue), Chapala (green), and Megh (black)] during the post-monsoon season in 2014 and 2015, along with the observed linear trend in SST (K per 50 years; shading). (b) Observed number of ESCSs over the ARB for each month for the period 1998–2016.

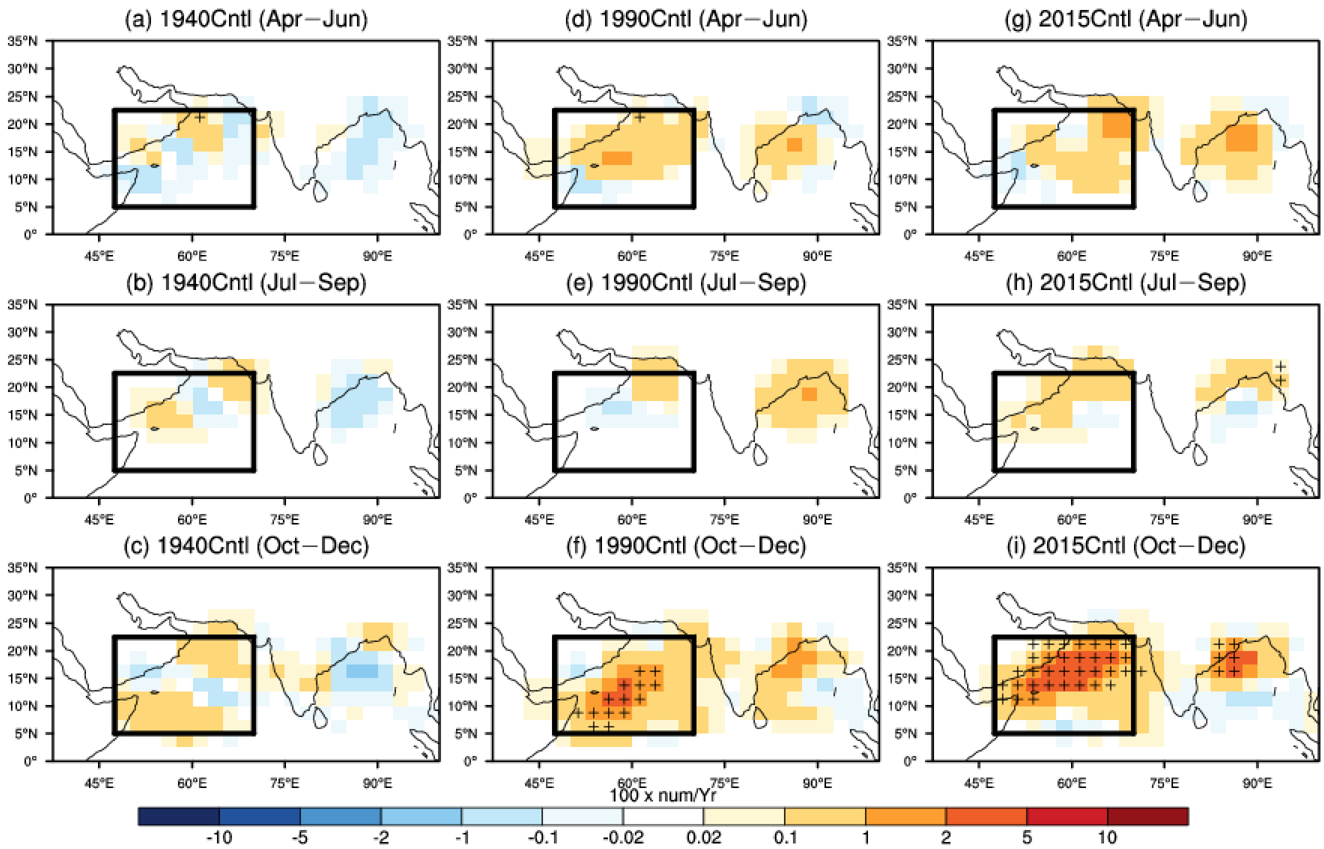

FIG. 2: Projected changes in the seasonal mean density of ESCSs. Projected changes in the seasonal mean density of ESCSs by 1940Cntl relative to 1860Cntl during the (a) pre-monsoon season (Apr–Jun), (b) peak monsoon season (Jul–Sep), and (c) post-monsoon season (Oct–Dec). (d–f) As in (a–c), but for 1990Cntl. (g–i) As in (a–c), but for 2015Cntl. Cross marks indicate the projected change relative to 1860Cntl is statistically significant at the 99% confidence level or above (boot strap method proposed by Murakami et al.[24]). Units: 100 × number year^{-1}. The black box highlights the domain of significant change in the post-season over the ARB.

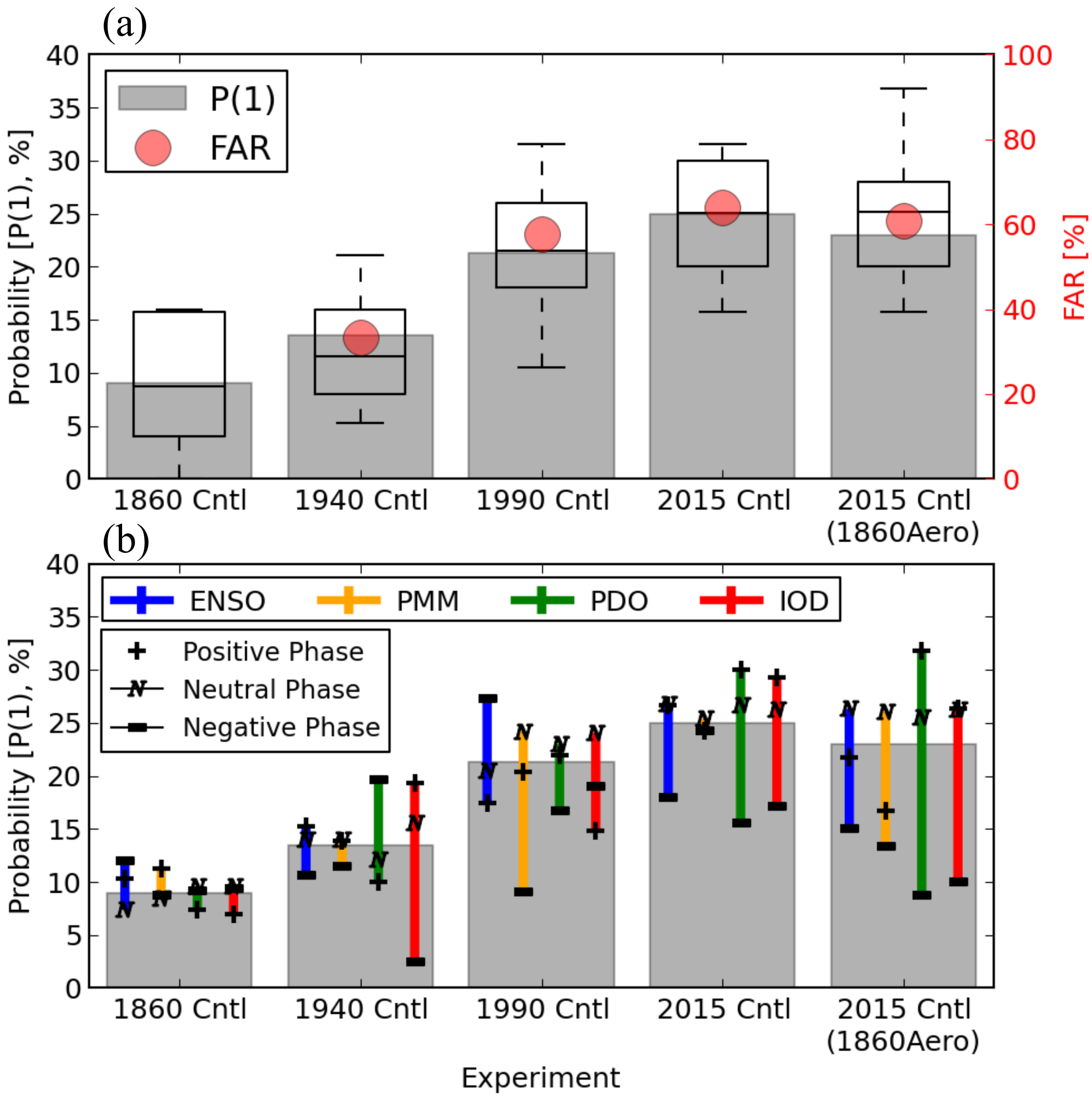

FIG. 3: Projected probability of exceedance of ESCSs over the ARB during October–December for each experiment. (a) *P(1)*, denoting the probability of occurrence of a year with the ESCS number greater than or equal to one during October–December, obtained by each control experiment using all simulation years (gray bars). The box plots represent uncertainty in *P(1)*. The boxes represent the range of the 10% and 90% quantiles of *P(1)* computed from 50-year periods; the horizontal lines show the median value; and the dashed bars show the 10% and 90% quantiles computed from 19-year periods. Red dots represent the FAR relative to 1860Cntl. (b) Gray bars are the same as in (a). Colored bars show the range of conditional *P(1)* induced by natural variability. The marks +, – and *N* indicate *P(1)* under the condition of a positive phase, negative phase, and neutral phase of natural variability, respectively. Evaluated natural variabilities are ENSO (blue), PMM (orange), PDO (green), and IOD (red). A positive (negative) phase is defined as when a climate index is greater than or equal to +0.75 (less than or equal to −0.75) standard deviation. Units: %.

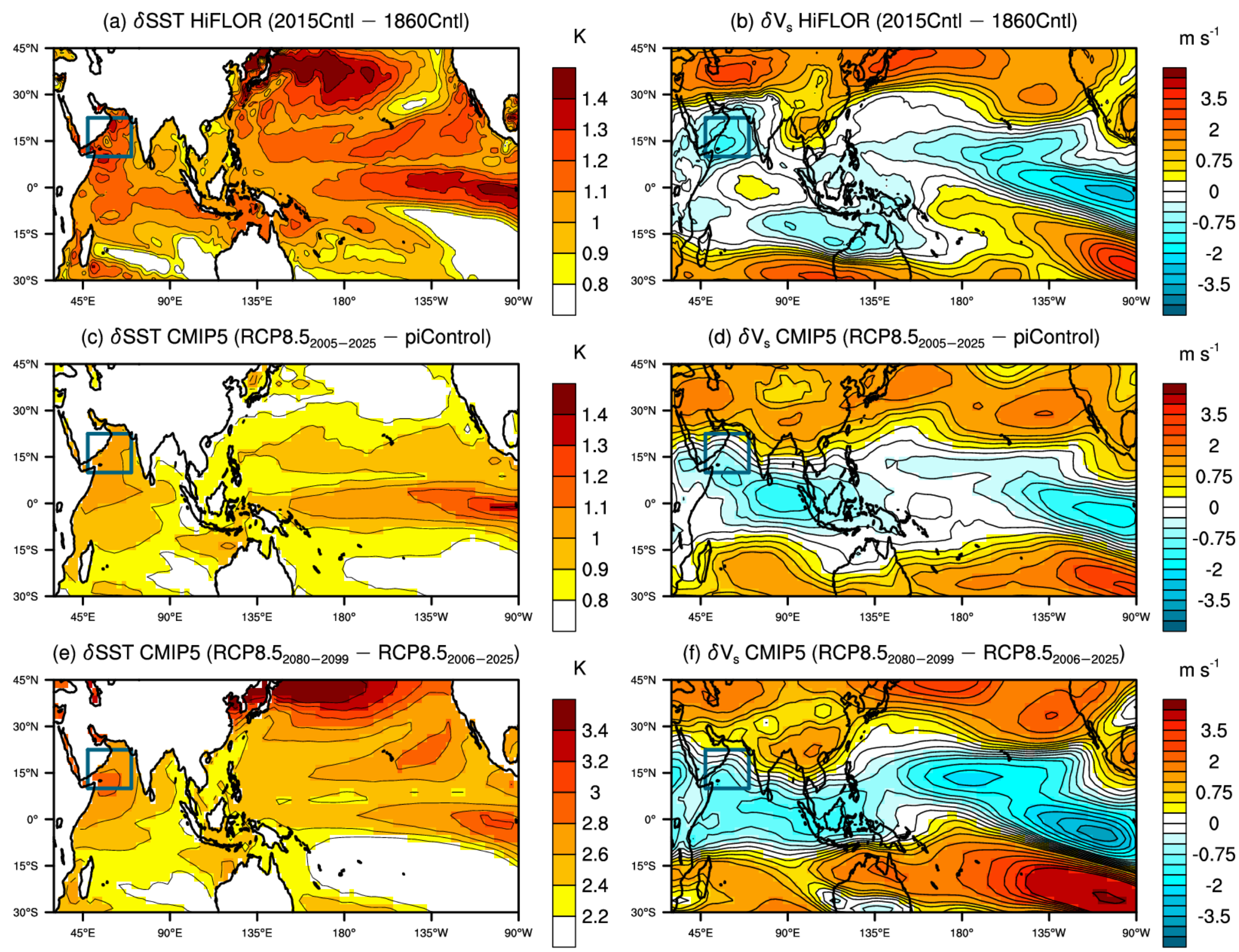

FIG. 4: Projected changes in seasonal mean SST and V_s. (a) Projected change in seasonal mean SST [K] by 2015Cntl relative to 1860Cntl, for October–December. (b) As in (a), but for V_s [m s^{-1}]. (c, d) As in (a, b), but for the ensemble mean of 22 CMIP5 models under the RCP8.5 scenario (2006–2025) relative to those of the pre-industrial control experiments (500 years). (e, f) As in (c, d), but for the mean difference between 2080–2099 and 2006–2025 projected by 36 CMIP5 models under the RCP8.5 scenario. The green rectangle is the domain over the ARB where ESCSs increased.